Supporting Information

Congfu Zhang, Zhaolu Wang, Changchang Zhang, Wenjuan Shi, Wei Li, Ke Gao, Hongjun Liu*

Contents

S1 Simulation Method

Numerical modeling is performed with the help of commercial software FDTD solutions (Lumerical) based on the finite difference time-domain method. We use the plane wave illumination source. For the metasurface structure, the periodic boundary condition in the x and y direction with a period of 1800 nm and the PML condition in the z direction are set, and the permittivities of Au and SiO_2 are from the Palik model, and the permittivity of ZnO is from ref. 35.

S2 Dispersion relations

We theoretically solved the dispersion relation for the trigonal structure. We equate the structure of a metal/dielectric multilayer to an HMM, whose optical properties are characterized by the equivalent dielectric constant (ε_{eff}) and the equivalent magnetic permeability (μ_{eff}). Here we do not consider the magnetic characterization of the material, and thus we can assume that $\mu_{eff} = 1$. For a two-dimensional air/HMM/air

structure, the electric field component E_z of the supported waveguide mode (TM mode) can be expressed as

$$E_z = A_1 \exp(-\gamma_1(x' - \frac{ay'}{2\tan\frac{\theta}{2}})) + B_1 \exp(\gamma_1(x' + \frac{a(y'-P)}{2\tan\frac{\theta}{2}} - P)) \quad -\tan\frac{\theta}{2}y + \frac{a}{2} < x < P \tag{S1}$$

$$E_z = C_1 \exp(-\gamma_1(x' - \frac{a(y'+P)}{2\tan\frac{\theta}{2}} + P)) + D_1 \exp(\gamma_1(x' + \frac{ay'}{2\tan\frac{\theta}{2}})) \quad \tan\frac{\theta}{2}y - \frac{a}{2} < x < -\tan\frac{\theta}{2}y + \frac{a}{2} \tag{S2}$$

$$E_z = F_1 \exp(i\gamma_2(x' - a\frac{y'}{2\tan\frac{\theta}{2}})) + G_1 \exp(-i\gamma_2(x' + a\frac{y'}{2\tan\frac{\theta}{2}})) \quad -P < x < \tan\frac{\theta}{2}y - \frac{a}{2} \tag{S3}$$

where $\gamma_1 = \sqrt{\beta^2 - \varepsilon_1 k_0^2}$, $\gamma_2 = \sqrt{\varepsilon_{zz}k_0^2 - \varepsilon_{zz}\beta^2/4\varepsilon_{xx} - \varepsilon_{zz}\beta^2/3\varepsilon_{yy}}$.

According to Maxwell's equations, the magnetic field component H_y can be expressed as

$$H_y = A_1\gamma_1\omega\varepsilon_1 \exp(\gamma_1(x' + \frac{a(y'-P)}{2\tan\frac{\theta}{2}})) - \gamma_1 B_1\omega\varepsilon_1 \exp(-\gamma_1(x' - \frac{ay'}{2\tan\frac{\theta}{2}})) \tag{S4}$$

$$H_y = -C_1\gamma_1\omega\varepsilon_1 \exp(-\gamma_1(x' - \frac{a(y'-P)}{2\tan\frac{\theta}{2}} + P)) + D_1\gamma_1\omega\varepsilon_1 \exp(\gamma_1(x' + \frac{ay'}{2\tan\frac{\theta}{2}})) \tag{S5}$$

$$H_y = iF_1\gamma_2\omega\varepsilon_{zz} \exp(i\gamma_2(x' - \frac{ay'}{2\tan\frac{\theta}{2}})) - iG_1\gamma_2\omega\varepsilon_{zz} \exp(-i\gamma_2(x' + \frac{ay'}{2\tan\frac{\theta}{2}})) \tag{S6}$$

the magnetic field component H_x are

$$H_x = A_1\gamma_1\omega\varepsilon_1 \frac{a}{2\tan\frac{\theta}{2}} \exp(\gamma_1(x' + \frac{a(y'-P)}{2\tan\frac{\theta}{2}})) + \gamma_1 B_1\omega\varepsilon_1 \frac{a}{2\tan\frac{\theta}{2}} \exp(-\gamma_1(x' - \frac{ay'}{2\tan\frac{\theta}{2}})) \tag{S7}$$

$$H_y = C_1\gamma_1\omega\varepsilon_1 \frac{a}{2\tan\frac{\theta}{2}} \exp(-\gamma_1(x' - \frac{a(y'-P)}{2\tan\frac{\theta}{2}} + P_x)) + D_1\gamma_1\omega\varepsilon_1 \frac{a}{2\tan\frac{\theta}{2}} \exp(\gamma_1(x' + \frac{ay'}{2\tan\frac{\theta}{2}})) \tag{S8}$$

$$H_y = iF_1\gamma_2\omega\varepsilon_{zz} \frac{a}{2\tan\frac{\theta}{2}} \exp(i\gamma_2(x' - \frac{ay'}{2\tan\frac{\theta}{2}})) - iG_1\gamma_2\omega\varepsilon_{zz} \frac{a}{2\tan\frac{\theta}{2}} \exp(-i\gamma_2(x' + \frac{ay'}{2\tan\frac{\theta}{2}})) \tag{S9}$$

Based on the boundary conditions

$$\begin{gathered} y' = 0, \quad y' = \frac{a}{2\tan\frac{\theta}{2}}, \quad x' = -\frac{a}{2}, \quad x' = 0; \\ y' = 0, \quad y' = \frac{a}{2\tan\frac{\theta}{2}}, \quad x' = \frac{a}{2}, \quad x' = 0; \\ y' = 0, \quad x' = -\frac{a}{2}, \quad x' = \frac{a}{2}. \end{gathered} \tag{S10}$$

The equations satisfy the continuity at the boundary conditions, and after calculation we can get the dispersion relation

$$\frac{\exp(-i\gamma_2 a/2\tan\frac{\theta}{2}) - \exp\left[\gamma_1\left(P - \frac{a}{2\tan\frac{\theta}{2}}\right)\right]}{\exp(i\gamma_2 a/2\tan\frac{\theta}{2}) - \exp\left[\gamma_1\left(P - \frac{a}{2\tan\frac{\theta}{2}}\right)\right]} = \frac{\exp(-i\gamma_2 a/2\tan\frac{\theta}{2}) - \exp\left[-\gamma_1\left(P - \frac{a}{2\tan\frac{\theta}{2}}\right)\right]}{\exp(i\gamma_2 a/2\tan\frac{\theta}{2}) - \exp\left[-\gamma_1\left(P - \frac{a}{2\tan\frac{\theta}{2}}\right)\right]}\left(\frac{\varepsilon_1\gamma_1 + i\varepsilon_z\gamma_2}{\varepsilon_1\gamma_2 - i\varepsilon_z\gamma_1}\right)^2 \tag{S11}$$

S3 Electric multipole in the round table and pyramid structure

In previous studies, researchers always used the round table and pyramid structures for light absorption, and therefore always studied the absorption enhancement caused by

the electric dipole and ignored the electric multipoles in front. The field distribution in the *x*-*y* plane for the wavelengths of these absorption peaks is shown in Fig. S1, and it can be found that these electric multipoles, in both structures, are unable to produce a field overlap with the mode field generated by the electric dipole, which is caused by their charge distribution.

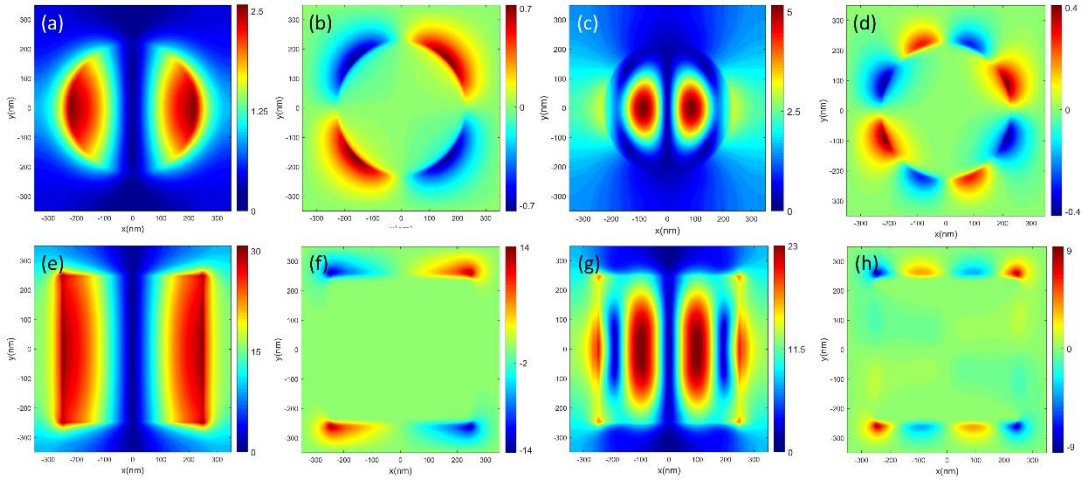

Figure S1 Field distribution |E| and E_x of cylindrical(a-d) and square structure(e-h)

S4 The multipolar decomposition spectra

We calculated the multipole decomposition of the scattering efficiency for a plane wave scattered on a triangular prism structure, the method comes from Ref. [1].

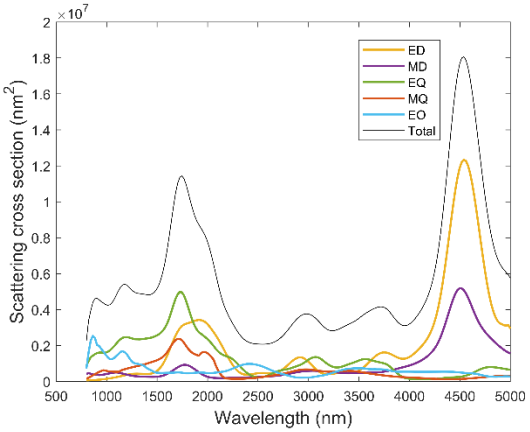

Figure S2 The multipolar decomposition spectra. ED, MD, EQ, MQ, EO represent electric dipole, magnetic dipole, electric quadrupole, magnetic quadrupole, and electric octupole respectively.

S5 The cause of the absorption peaks

We plotted the electric field distributions of absorption peaks 2 and 3 in Figure 7 of the absorption spectrum, and the locations are consistent with absorption peak 4. The main reason for peak 2 is the electric quadrupole and electric dipole and its hybridization, peak 3 is mainly due to the electric quadrupole and electric hexapole and its hybridization.

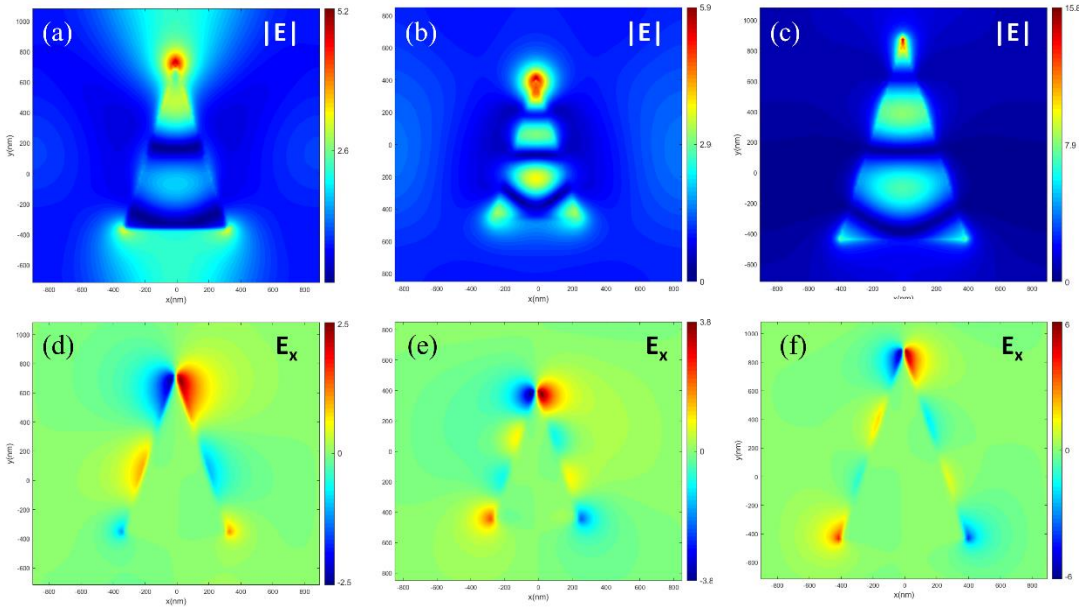

Figure S3 Distribution of electric field |E|, E_x for absorption peak 2 in the absorption spectrum, (a, d) layer 4 (b, e) layer 6 (c, f) layer 9.

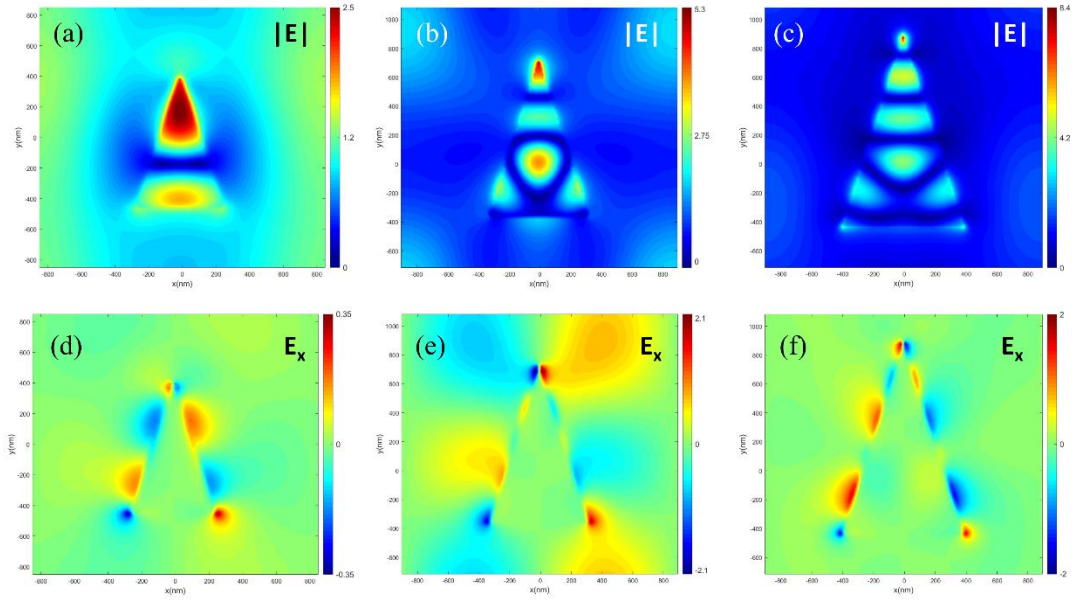

Figure S4 Distribution of electric field |E|, E_x for absorption peak 3 in the absorption spectrum, (a, d) layer 4 (b, e) layer 6 (c, f) layer 9

S6 Sum frequency generation in triangular pyramidal structures

The 6 mm symmetry of the ZnO wurtzite crystal structure supports five nonzero elements of the second order nonlinear susceptibility tensor (written in d matrix notation):

$$\chi^{(2)}_{\mathrm{ZnO}}=\begin{pmatrix}0&0&0&0&\chi_{15}&0\\0&0&0&\chi_{24}&0&0\\\chi_{31}&\chi_{32}&\chi_{33}&0&0&0\end{pmatrix} \tag{S12}$$

Then the polarization intensity in ZnO can be expressed as

$$\begin{pmatrix}P_x(\omega_c)\\P_y(\omega_c)\\P_z(\omega_c)\end{pmatrix}=\varepsilon_0\begin{pmatrix}0&0&0&0&\chi_{15}&0\\0&0&0&\chi_{24}&0&0\\\chi_{31}&\chi_{32}&\chi_{33}&0&0&0\end{pmatrix}\begin{pmatrix}E_x(\omega_s)E_x(\omega_p)\\E_y(\omega_s)E_y(\omega_p)\\E_z(\omega_s)E_z(\omega_p)\\E_y(\omega_s)E_z(\omega_p)+E_z(\omega_s)E_y(\omega_p)\\E_x(\omega_s)E_z(\omega_p)+E_z(\omega_s)E_x(\omega_p)\\E_x(\omega_s)E_y(\omega_p)+E_y(\omega_s)E_x(\omega_p)\end{pmatrix} \tag{S13}$$

$$P_x(\omega_c)=\varepsilon_0\chi_{15}\left[E_x(\omega_s)E_z(\omega_p)+E_z(\omega_s)E_x(\omega_p)\right] \tag{S14}$$

$$P_y(\omega_c)=\varepsilon_0\chi_{24}[E_y(\omega_s)E_z(\omega_p)+E_z(\omega_s)E_y(\omega_p)] \tag{S15}$$

$$P_z(\omega_c)=2\varepsilon_0\chi_{31}\left[E_x(\omega_s)E_x(\omega_p)+E_y(\omega_s)E_y(\omega_p)\right]+\varepsilon_0\chi_{33}E_z(\omega_s)E_z(\omega_p) \tag{S16}$$

S7 Influence of signal beam wavelength variation on SFG emission

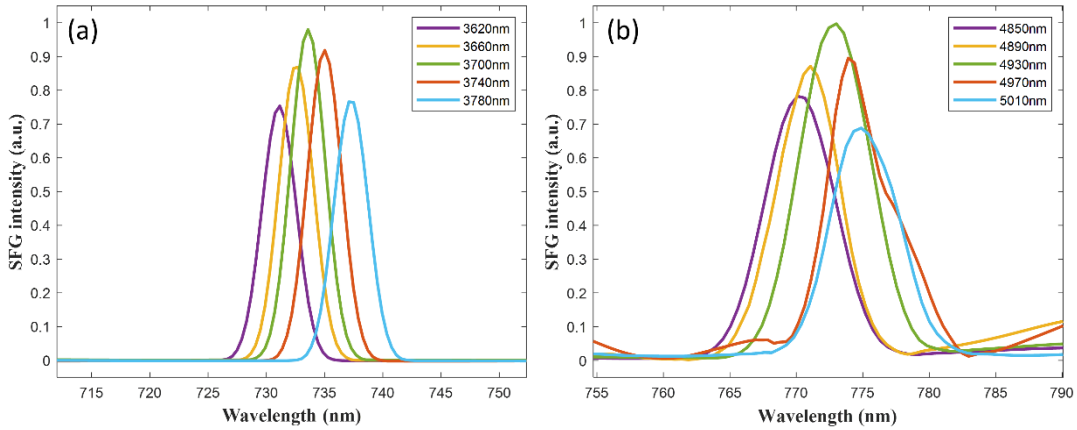

Figure S5 Spectral dependence of the SFG emission on the varying wavelength of (a) the signal beam from 3620 to 3780 nm, and (b) the signal beam from 3080 to 3240 nm

S8 Different electric field components of upconversion light in *x-y* plane

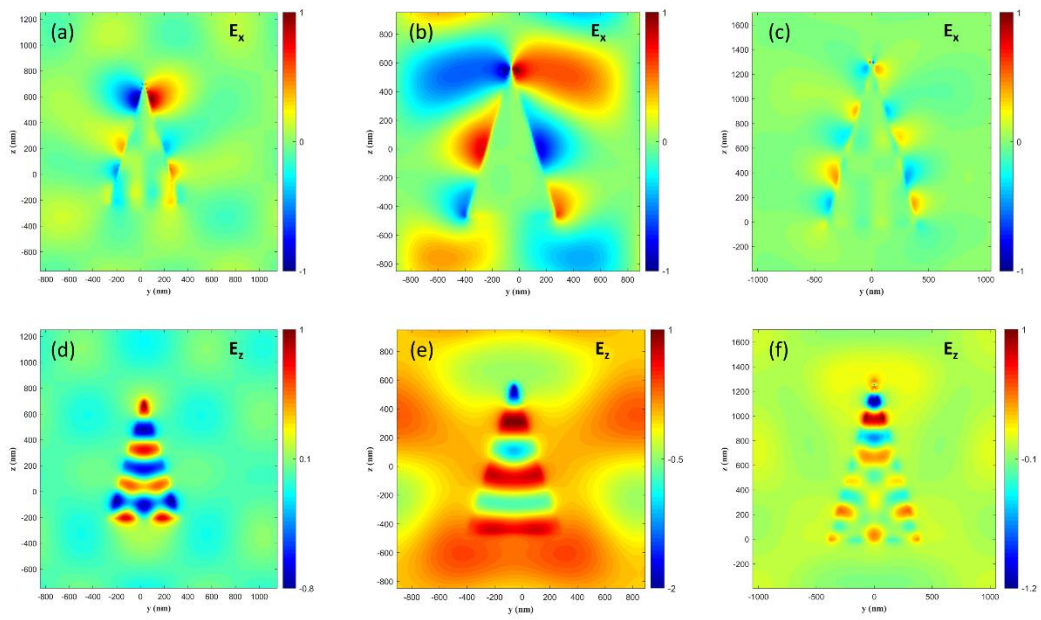

Figure S6 The distribution of E_x and E_z electric field in the *x*-*y* plane of the triangular pyramidal structure at different upconversion wavelengths. (a, d) 710nm; (b, e) 734nm (c, f) 772nm.

S9 Overlap integrals

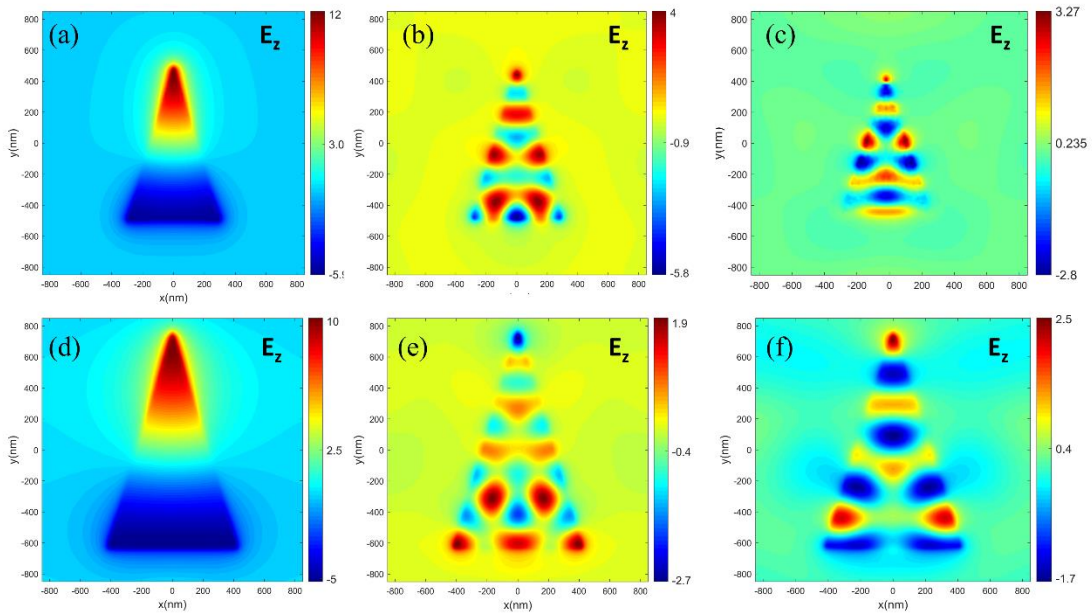

Figure S7 The distribution of E_z electric field in the *x*-*y* plane of the triangular pyramidal structure in layer 4 at wavelengths (a) 3700 nm; (b) 916 nm; (c) 732 nm; (d) 4930 nm; (e) 916 nm; (f) 780 nm.

S10 Influence of signal beam intensity on SFG emission

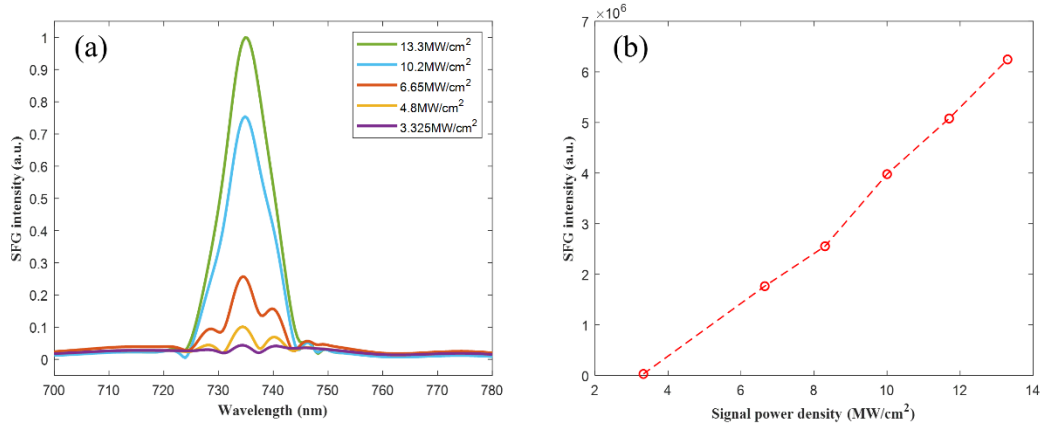

Figure S8 (a) The relationship between SFG emission intensity and spectrum at different signal intensities at 3700 nm. (b) The relationship between maximum SFG emission intensity and signal intensity at 3700 nm.

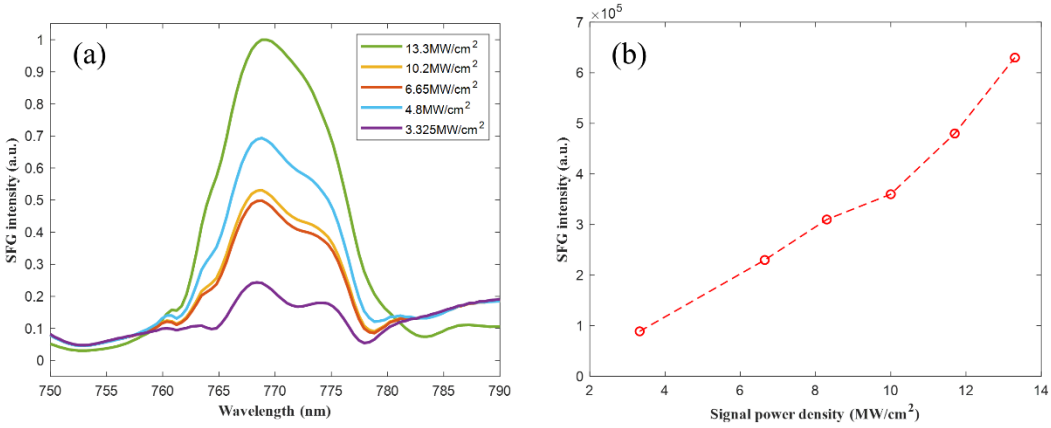

Figure S9 (a) The relationship between SFG emission intensity and spectrum at different signal intensities at 4930 nm. (b) The relationship between maximum SFG emission intensity and signal intensity at 4930 nm.

S11 Influence of components ratio of dielectric on linear and nonlinear properties of structures

The properties of the structure will be changed when the component ratios of the medium and the metal are changed. We have investigated the absorption spectra and effective nonlinear permittivity at different ratio through the effective medium theory.

When we consider only the incident light in the z direction, the effective nonlinear permittivity can be calculated through[2]:

$$\chi_{eff}^{(2)}=\frac{\dfrac{f_d\chi_d^{(2)}}{\varepsilon_d(\omega_{up})\varepsilon_d(\omega_s)\varepsilon_d(\omega_p)}+\dfrac{f_m\chi_m^{(2)}}{\varepsilon_m(\omega_{up})\varepsilon_m(\omega_s)\varepsilon_m(\omega_p)}}{\left(\dfrac{f_d}{\varepsilon_d(\omega_s)}+\dfrac{f_m}{\varepsilon_m(\omega_s)}\right)\left(\dfrac{f_d}{\varepsilon_d(\omega_p)}+\dfrac{f_m}{\varepsilon_m(\omega_p)}\right)\left(\dfrac{f_d}{\varepsilon_d(\omega_{up})}+\dfrac{f_m}{\varepsilon_m(\omega_{up})}\right)} \tag{S17}$$

We simulate the relationship between the effective nonlinear permittivity and the ratio of dielectric components. It can be seen that although the effective nonlinear dielectric constant increases nearly three times (for $f_d = 0.75$) when the dielectric component ratio

is increased, the conversion efficiency does not increase, and this is due to the fact that the increase of the dielectric component ratio weakens the FP effect in the optical cavity, which decreases the enhancement of the electric field, and at this time, the overlap of the mode fields is not good, which results in the decrease of the conversion efficiency.

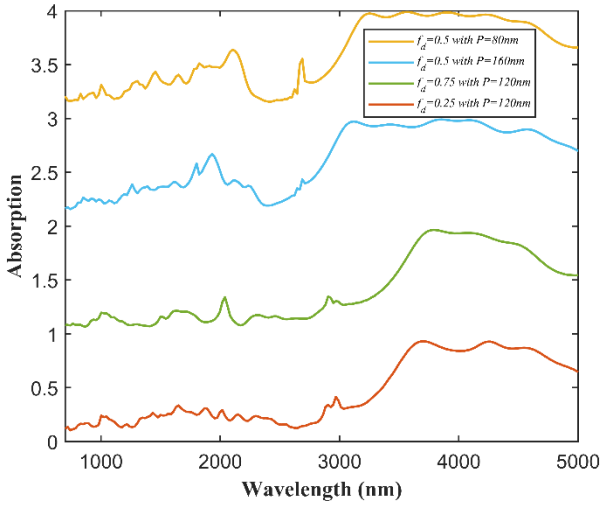

Figure S10 the absorption spectrum with different components ratio of dielectric.

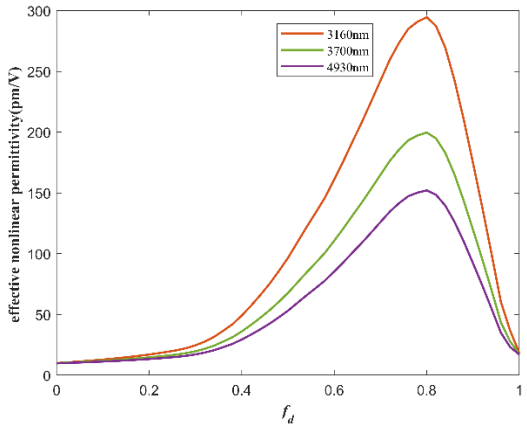

Figure S11 the relationship between the effective nonlinear permittivity and the ratio of dielectric components

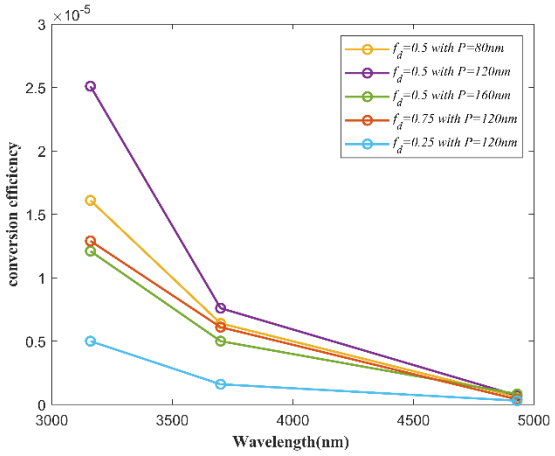

Figure S12 the nonlinear conversion efficiency with different ratio of dielectric

components

S12 The polarization dependence of different signal beams

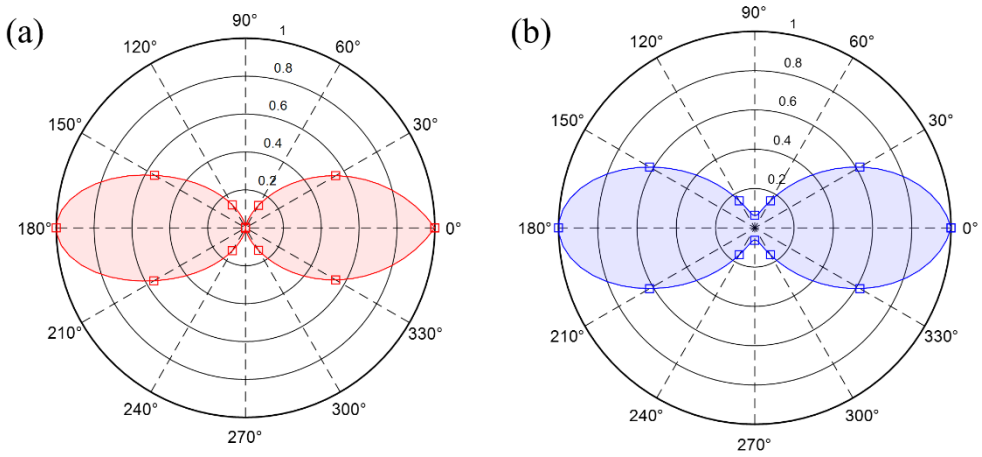

Figure S13 Polarization dependence of the SFG emission with λs=3700 nm. (a) the polarization of signal; (b) the polarization of pump.

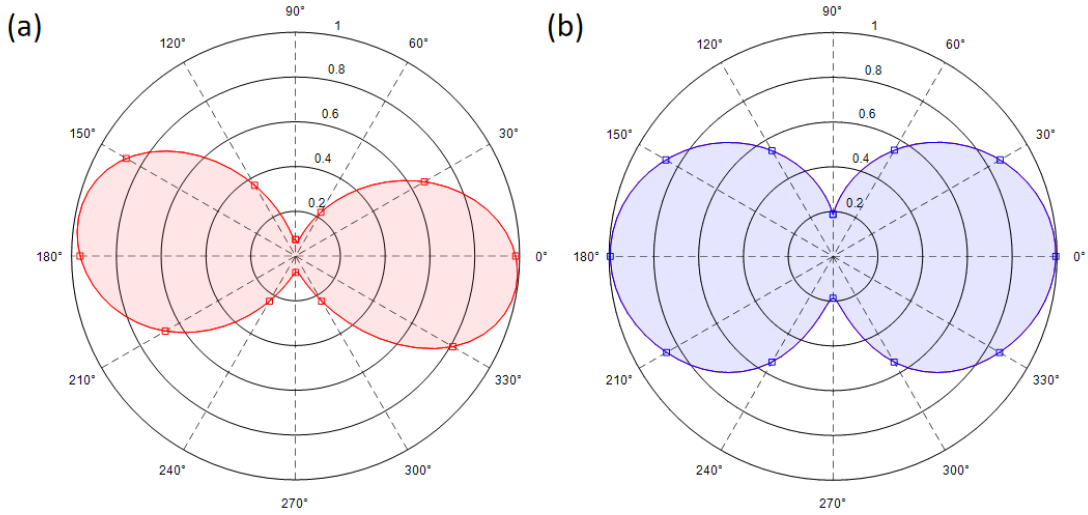

Figure S14 Polarization dependence of the SFG emission with λs=4930 nm. (a) the polarization of signal; (b) the polarization of pump.

S13 The maximum and minimum SFG emission are calculated under continuous signal wave

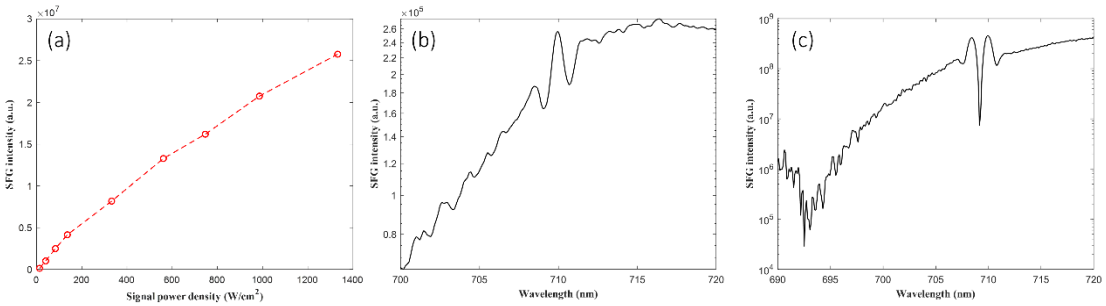

Figure S15 (a)Influence of continuous signal light intensity on SFG; (b) Minimum; (c) Maximum 710 nm SFG emissions are obtained for continuous signal wave.

S14 A comparison of the upconversion process through SFG method.

Table 1 | Summary of the SFG in the metasurface

Material	Method	Structure	Wavelength	Efficiency	Reference
GaAs	Mie resonance	Cylinder	1530nm	5×10^{-8}	[3]
Au-Al_2O_3	SPP	MIM	1470-1530nm	-	[4]
Graphene-gold	Magnetic Lorentz force	SRR	30THz	8.2×10^{-7}	[5]
AlGaInP-Al_2O_3-Ag	Hybrid plasmonic modes	Nanowire	1320nm	14.8% MW^{-1}	[6]
$LiNbO_3$-SiO_2	GMR	Grating	1530nm	$1.93\times10^{-5}cm^2\ GW^{-1}$	[7]
GaSe-Si	TD resonance	Thin layer	10μm and 16μm	1.6×10^{-7}	[8]
GaP	BIC	Ellipse	1545nm	$2.5\times10^{-4}W^{-1}$	[9]
Au-ZnO	**Gap-plasma modes**	**Triangular pyramidal**	**3000-5000nm**	**2.5×10^{-5}**	**This Work**

S15 The effect of fabrication error

We provide possible fabrication methods and add them to the supplementary materials. This method is obtained according to the Ref. [10], who have fabricated multilayer structures of various shapes using this method.

(1), Zinc oxide (ZnO) and gold films are deposited sequentially on a silicon substrate using a magnetron sputtering system until the number of deposited layers meets the design requirements;

(2), After spin-coating with resist, the multilayered Au−ZnO film was exposed by electron beam lithography, nanoimprint, laser direct writing, or ultraviolet (UV) exposure to form the hole arrays;

(3) the hole pattern was transferred to aluminum truncated-cone-type array by the electron beam evaporation and lift-off processes;

(4) Subsequently, the IBE was performed to transfer the truncated-cone-type nanostructure to the Au−ZnO multilayered film (Figure 1d), whose bevel angles are mainly dependent on the bevel angle and thickness of deposited mask as well as the etching parameters of IBE (e.g., etching incidence angle and ion energy);

(5) The residual mask material was removed to obtain a triangular prismatic multilayer metamaterial with inclined angles.

Regarding the effect of fabrication error, we simulated the effect of fabricated surface roughness and disappearance of sharp corners on the results. For the surface roughness error, we change the structure size of each layer to a triangular prism structure with the same size of the upper and lower bottoms, and for the sharp corner vanishing error, we change the sharp corner to rounded corner and set up a slight asymmetry between left and right structures.

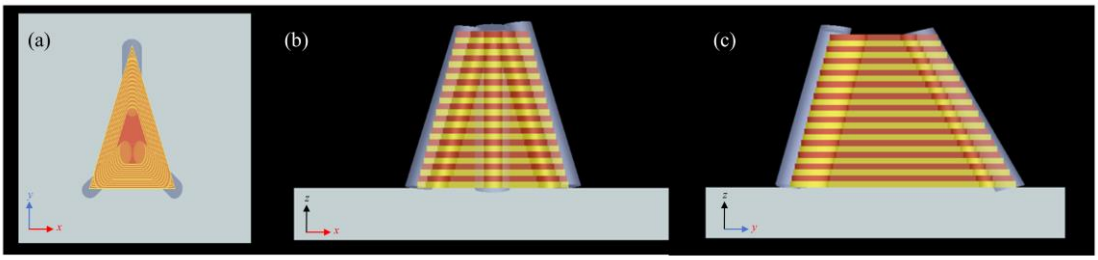

Fig S16 Simulation structure of fabrication error

The structure is shown in Fig. S16, and the absorption spectra are shown in Fig. S17(a), which can be seen that at this time the high absorption band decreases at large wavelengths, and there is a slight attenuation and redshift for the front absorption peak.

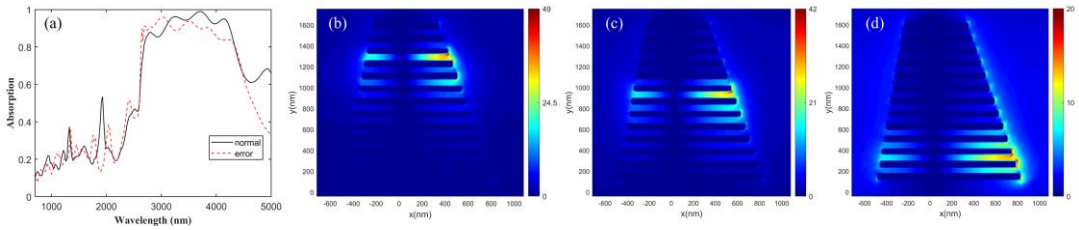

Fig. S17 (a) Black line is the absorption spectrum without error and red line is the absorption spectrum with error; Distributions of electric field |E| in the *y*-*z* plane of the triangular pyramidal at different incident wavelengths, specifically 3160 nm (b), 3700 nm (c), and 4930 nm (d).

As for the field enhancement, as shown in Fig. S17(b-d), which is shown that the field enhancement decreases at the resonance peak. In addition, the field distributions of the signaling pump light and the upconverted light are shown in Fig. S18, while we calculated the nonlinear conversion efficiencies for 3160 nm, 3700 nm, and 4930 nm, and the conversion efficiencies of 1.2×10^{-5}, 4.4×10^{-7} and 9.2×10^{-8} are calculated respectively, suggesting that fabrication errors weaken the nonlinear processes in the structure, but the effect is not significant.

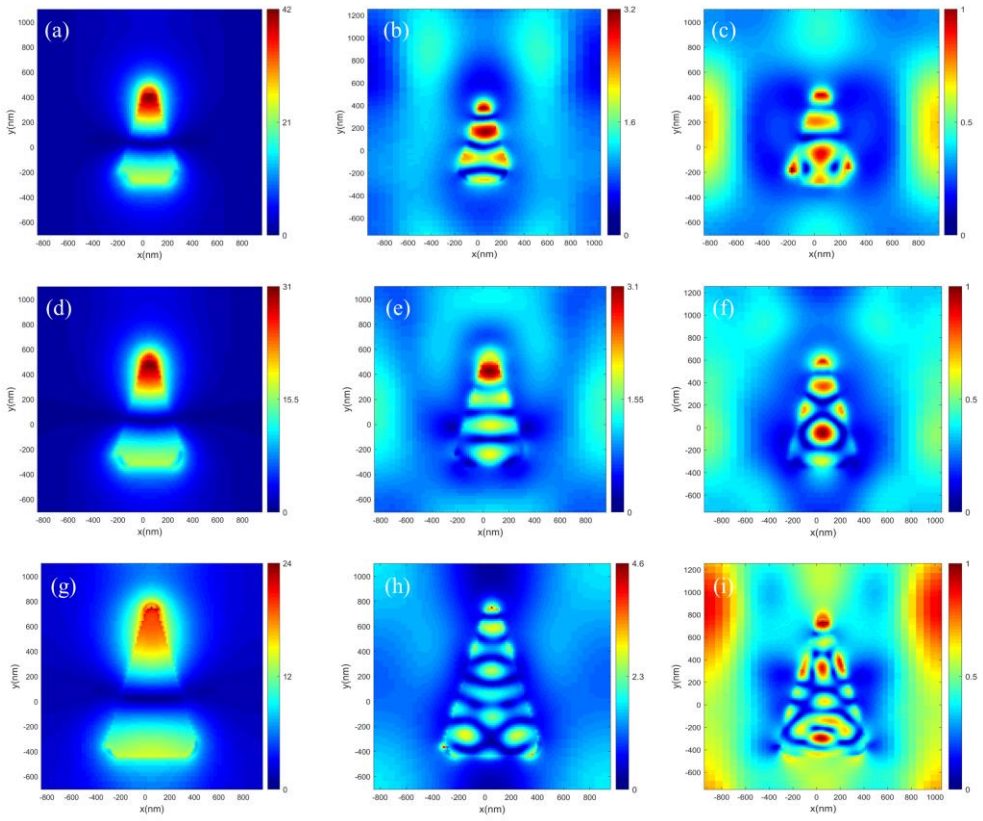

Fig. S18 Distributions of electric field |E| in the *x*-*y* plane at different signal wavelengths, specifically 3160 nm (a), 3700 nm (d), 4930 nm (g), pump wavelength 916nm (b, e, h), and the upconversion wavelength710 nm (c), 734 nm (f), and 772 nm (i) (normalized).

Reference

1. E. A. Gurvitz, K. S. Ladutenko, P. A. Dergachev, A. B. Evlyukhin, A. E. Miroshnichenko and A. S. Shalin, "The High-Order Toroidal Moments and Anapole States in All-Dielectric Photonics," Laser & Photonics Reviews **13**(5), 13 (2019)

2. R. W. Boyd and J. E. Sipe, "NONLINEAR-OPTICAL SUSCEPTIBILITIES OF LAYERED COMPOSITE-MATERIALS," Journal of the Optical Society of America B-Optical Physics **11**(2), 297-303 (1994)

3. R. Camacho-Morales, D. Rocco, L. Xu, V. F. Gili, N. Dimitrov, L. Stoyanov, Z. H. Ma, A. Komar, M. Lysevych, F. Karouta, A. Dreischuh, H. H. Tan, G. Leo, C. De Angelis, C. Jagadish, A. E. Miroshnichenko, M. Rahmani and D. N. Neshev, "Infrared upconversion imaging in nonlinear metasurfaces," Advanced Photonics **3**(3), 10 (2021)

4. S. G. Bai, M. Fang, W. E. I. Sha, Y. R. Qu, Z. W. Jin, J. Y. Tian, K. K. Du, S. L. Yu, C. W. Qiu, M. Qiu and Q. Li, "Chip-Scale Plasmonic Sum Frequency Generation," Ieee Photonics Journal **9**(3), 8 (2017)

5. J. Yao, G. X. Cai, N. Liu and Q. H. Liu, "Enhancing artificial sum frequency generation from graphene-gold metamolecules," Optics Letters **43**(13), 3160-3163 (2018)

6. Z. Li, B. Corbett, A. Gocalinska, E. Pelucchi, W. Chen, K. M. Ryan, P. Khan, C. Silien, H. X. Xu and

N. Liu, "Direct visualization of phase-matched efficient second harmonic and broadband sum frequency generation in hybrid plasmonic nanostructures," Light-Science & Applications **9**(1), 10 (2020)
7. L. V. Molina, R. C. Morales, J. H. Zhang, R. Schiek, I. Staude, A. A. Sukhorukov and D. N. Neshev, "Enhanced Infrared Vision by Nonlinear Up-Conversion in Nonlocal Metasurfaces," Advanced Materials, 9 (2024)
8. X. Hu, N. Li, W. Hong, G. H. Gu, Q. Chen and X. B. Sui, "Long-wave infrared to short-wave infrared upconversion through sum-frequency generation in a silicon symmetric metasurface integrated with two-dimensional material," Applied Surface Science **611**, 7 (2023)
9. R. C. Camacho-Morales, L. Xu, H. Z. Zhang, S. T. Ha, L. Krivitsky, A. I. Kuznetsov, M. Rahmani and D. Neshev, "Sum-Frequency Generation in High-Q GaP Metasurfaces Driven by Leaky-Wave Guided Modes," Nano Letters, 8 (2022)
10. T. Cao, C.-w. Wei, R. E. Simpson, L. Zhang and M. J. Cryan, "Broadband Polarization-Independent Perfect Absorber Using a Phase-Change Metamaterial at Visible Frequencies," Scientific Reports **4**(1), 3955 (2014)